



Article

First-Principles Investigation on Phase Stability, Mechanical Properties, Bonding Characteristic and Slip Properties of Ti-Co Binary Intermetallic Compounds

Fanlin Zeng ^{1,2} , Mengjie Chen ², Hongbo Wang ², Hexiang Peng ², Bei Li ^{1,*} and Jian Huang ^{2,*} ¹ School of Materials Science and Engineering, Wuhan University of Technology, Wuhan 430070, China² State Key Laboratory of High Performance Ceramics and Superfine Microstructure, Shanghai Institute of Ceramics, Chinese Academy of Sciences, Shanghai 201899, China

* Correspondence: libei@whut.edu.cn (B.L.); jhuang@mail.sic.ac.cn (J.H.)

Abstract: Ti-Co binary intermetallic compounds have attracted lots of attention due to their excellent toughness and interesting anomalous ductility. However, systematic theoretical calculations of alloy properties of different Ti-Co compounds have not been properly investigated yet. In this work, first-principles calculations were performed to study the phase stability, mechanical properties bonding characteristic and slip properties of five Ti-Co binary compounds. The negative enthalpy of formation and cohesive energy showed that all the Ti-Co binary compounds were thermodynamically stable, and TiCo is the most mechanically stable one. According to the elastic stability criterion, these compounds are also mechanically stable. In addition, the mechanical anisotropy of Ti-Co compounds was analyzed by the anisotropy index and the three-dimensional surface of Young's modulus, where Ti₂Co shows the strongest anisotropy, and TiCo₂(h) has weakest anisotropy. The phonon calculations of these compounds also show that all five Ti-Co compounds are thermodynamically stable. The density of states (DOS) and differential charge density distributions were analyzed to identify the chemical bonding characteristics of the Ti-Co binary compounds, which exhibit metal and covalent-like bonding and different magnetic properties. Finally, the plastic deformation mechanism of Ti-Co compounds was understood by calculating the generalized stacking fault energy (GSFE) of different slip systems. The anomalous ductility of TiCo and TiCo₃ mainly arises from the complex slip system and the lower slip energy barrier of the compounds.

Keywords: Ti-Co binary intermetallic compounds; phase stability; phonon properties; slip system; first-principles



Citation: Zeng, F.; Chen, M.; Wang, H.; Peng, H.; Li, B.; Huang, J. First-Principles Investigation on Phase Stability, Mechanical Properties, Bonding Characteristic and Slip Properties of Ti-Co Binary Intermetallic Compounds. *Metals* **2023**, *13*, 628. <https://doi.org/10.3390/met13030628>

Academic Editor: Alain Pasturel

Received: 21 February 2023

Revised: 16 March 2023

Accepted: 17 March 2023

Published: 21 March 2023



Copyright: © 2023 by the authors. Licensee MDPI, Basel, Switzerland. This article is an open access article distributed under the terms and conditions of the Creative Commons Attribution (CC BY) license (<https://creativecommons.org/licenses/by/4.0/>).

1. Introduction

Ti-Co binary intermetallic compounds have garnered extensive attention in the medical and aerospace industries due to their good oxidation resistance at high temperatures, corrosion resistance, unique shape memory properties and good phase stability [1–7]. Ti-Co alloys have been used extensively as implant alloys in dentistry and medicine for many years [5,7,8]. Thus, Ti-based alloys with additions of cobalt show more strength and have lower melting temperature, which can alleviate many casting problems [9]. The addition of cobalt improves the corrosion resistance of titanium and its mechanical properties [10]. Ternary (Ti-Co)-based alloys have also been used in many applications [11,12]. Ti-Co alloys are frequently used as coatings on other titanium alloys such as Ti6Al4V [13]. Such surface modifications allow the improved durability of Ti6Al4V alloy due to the formation of hard Ti-Co intermetallic particles. Ti-Co thin films are also used as diffusion barriers or as an element in integrated circuits [14,15]. In high-temperature Co-based superalloys, Ti-Co compounds are regarded as the only thermodynamically stable phases, because Ti in Co-based superalloys can stabilize the γ' phase at high temperatures, thereby improving the high-temperature oxidation resistance and mechanical properties [2–4,6,16,17].

Recently, many experimental and theoretical studies have been conducted to study the phase diagram, preparation, thermodynamics and mechanical properties of Ti-Co binary compounds [18–24]. Murray [18] systematically studied the phase diagram of Ti-Co. Cacciamani et al. [24] and Davydov et al. [20] developed a thermodynamic database of Ti-Co binary compounds system, and Xue et al. [21] prepared Ti-Co binary compounds by laser melting deposition. According to the phase diagram [18,24], there are five intermetallic compounds in the Ti-Co binary system: Ti_2Co , TiCo, Laves phase C15 (TiCo_2), Laves phase C36 (TiCo_2) and TiCo_3 . In terms of theoretical calculation, the crystal structure, electronic structure and elastic properties of TiCo and TiCo_3 have been extensively studied [25–29]. However, there have been no studies on Ti_2Co , $\text{TiCo}_2(\text{c})$ and $\text{TiCo}_2(\text{h})$, and comparisons of the phase stability, mechanical properties, thermodynamics and bonding characteristic of these compounds still are lacking. For Ti-Co binary compounds, no studies have been carried out to understand the thermodynamic stability of the structure of the phonon and to study the mechanical properties of the phase structure by calculating the stacking fault energy of different slip systems. The phonon properties of alloys provide information on the vibrations of the lattice and it allows us to acquire a better understanding of the microscopic properties of the material [30]. The GSFE surface quantifies the energy per unit area required to shear a crystal on a potential slip plane parallel to the displacement vector, which provides a significant insight into the mechanical properties [31]. The study of phonons and GSFE allows the macroscopic properties of Ti-Co binary compounds to be understood at the microscopic level.

Therefore, the phase stability, mechanical properties, bonding characteristics and slip properties of Ti-Co binary compounds were investigated using the first-principles calculation in this study. The phonon properties of Ti-Co binary compounds were studied by the frozen phonon method, and the generalized stacking fault energy (GSFE) was also calculated by constructing different structural models of the alloys. The results of this work can provide useful theoretical basis and prediction information for designing new Ti-Co alloys in the future.

2. Computational Methods

First-principles calculations were carried out using density functional theory (DFT) via the Vienna Ab initio simulation package (VASP) [32,33] with the projection augmented plane wave (PAW) [34] method. The Perdew–Bourke–Erzerhof (PBE) [35] pseudopotential in the form of generalized gradient approximation (GGA) was used to treat the exchange correlation energy between electrons in Ti-Co alloy system. The valence electrons of Ti and Co are $3p^6 3d^2 4s^2$ and $3s^2 3p^6 3d^7 4s^2$, respectively. According to the convergence test, the cutoff energy was set to 520 eV. The equilibrium crystal structure and atomic positions of each compound were relaxed using the conjugate gradient algorithm. The convergence criteria of force and energy were $0.01 \text{ eV}/\text{\AA}$ and 10^{-6} eV , respectively. According to the Ti-Co phase diagram [18,24], there are eight phases: hexagonal (α -Ti and $\text{TiCo}_2(\text{h})$), face-centered cubic (Ti_2Co , $\text{TiCo}_2(\text{c})$ and TiCo_3) and body-centered cubic (β -Ti, TiCo and α -Co) lattice, whose crystal structures are shown in Figure 1. The Monkhorst–Pack scheme was used for k-point sampling in the first irreducible Brillouin zone [36]: $12 \times 12 \times 5$, $6 \times 6 \times 1$, $4 \times 4 \times 4$, $6 \times 6 \times 6$, $8 \times 8 \times 8$, $10 \times 10 \times 10$, $8 \times 8 \times 8$, $9 \times 9 \times 9$ for each phase.

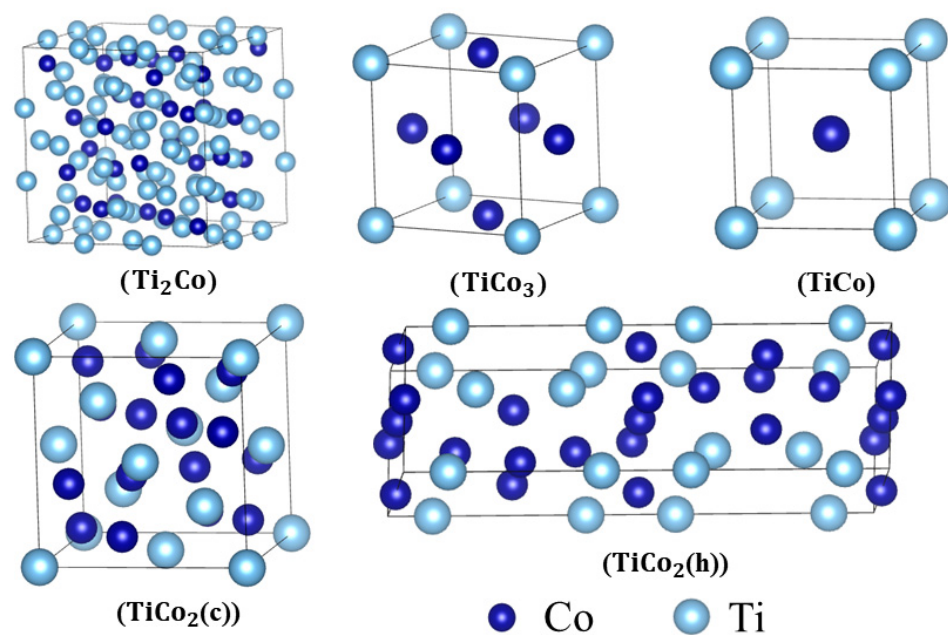


Figure 1. Crystal structures of Ti-Co binary compounds.

3. Results and Discussion

3.1. Lattice Parameters and Phase Stability

Table 1 shows the calculated lattice parameters, density, cohesive energy and enthalpy of formation of five Ti-Co binary compounds and Ti and Co, and it is shown that the lattice parameters match well with the experimental and other calculated ones, with an error of within 2%. The formation enthalpy and cohesive energy were used to characterize the stability of the alloy, and these were [37]:

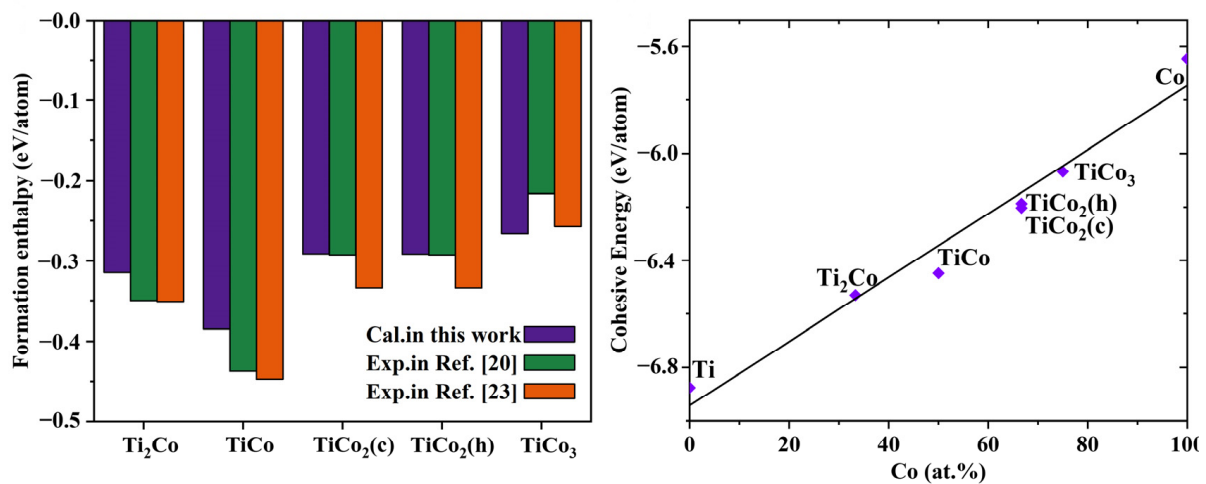
$$\Delta H_f(Ti_xCo_y) = \frac{E_{tol}(Ti_xAl_y) - xE_{coh}(Ti) - yE_{coh}(Co)}{x + y} \quad (1)$$

$$E_{coh}(Ti_xCo_y) = \frac{E_{tol}(Ti_xAl_y) - xE_{iso}(Ti) - yE_{iso}(Co)}{x + y} \quad (2)$$

where $\Delta H_f(Ti_xCo_y)$ is the formation enthalpy of Ti_xCo_y , $E_{coh}(Ti_xCo_y)$ is the cohesive energy of Ti_xCo_y , $E_{tol}(Ti_xAl_y)$ is the total energy of Ti_xCo_y , and $E_{coh}(Ti)$ and $E_{coh}(Co)$ are the cohesive energies of Ti and Co crystals, respectively, and $E_{iso}(Ti)$ and $E_{iso}(Co)$ is the energy of a single atom. The formation enthalpy and cohesive energy of all Ti-Co compounds are negative, indicating that these compounds are inherently thermodynamically stable. The formation enthalpy and cohesive energy as functions of the Co content are shown in Figure 2. The enthalpy of formation decreases initially, and then increased with the Co content, agreeing well with previous experimental results [20,23], while the cohesive energy increases with Co content, indicating a decreasing bonding strength between Ti and Co. Moreover, the lowest enthalpy of formation was -0.385 eV/atom for TiCo, signifying that TiCo is the most stable one in thermodynamics, followed by Ti_2Co .

Table 1. Crystal structure, density, cohesive energy, enthalpy of formation of Ti-Co phases, Ti and Co.

| Phase | Space Group | Strukturbericht Designation | Lattice Parameters | | | ρ (g/cm ³) | E_{coh} (eV/atom) | ΔH_f (eV/atom) |
|-----------------------|--------------|-----------------------------|--------------------|--------------------|--------------------|-----------------------------|---------------------|------------------------|
| | | | a (Å) | b (Å) | c (Å) | | | |
| β -Ti | $Im\bar{3}m$ | A2 | 3.25 | 3.25 | 3.25 | 4.58 | −6.88 | 0 |
| α -Ti | $P6_3/mmc$ | A3 | 3.31 ^a | 3.31 ^a | 3.31 ^a | 4.62 | −6.88 | 0 |
| | | | 2.94 | 2.94 | 4.65 | | | |
| Ti ₂ Co | $Fd\bar{3}m$ | | 2.95 ^a | 2.95 ^a | 4.68 ^a | 5.82 | −6.53 | −0.32 |
| | | | 11.22 | 11.22 | 11.22 | | | |
| TiCo | $Pm\bar{3}m$ | B2 | 11.30 ^b | 11.30 ^b | 11.30 ^b | 6.71 | −6.45 | −0.39 |
| | | | 2.92 | 2.92 | 2.92 | | | |
| TiCo ₂ (c) | $Fd\bar{3}m$ | C15 | 2.99 ^b | 2.99 ^b | 2.99 ^b | 7.52 | −6.20 | −0.29 |
| | | | 6.63 | 6.63 | 6.63 | | | |
| TiCo ₂ (h) | $P6_3/mmc$ | C36 | 6.72 ^b | 6.72 ^b | 6.72 ^b | 7.48 | −6.21 | −0.29 |
| | | | 4.70 | 4.70 | 15.29 | | | |
| TiCo ₃ | $Pm\bar{3}m$ | L1 ₂ | 4.73 ^b | 4.73 ^b | 15.43 ^b | 7.95 | −6.07 | −0.27 |
| | | | 3.60 | 3.60 | 3.60 | | | |
| α -Co | $Fm\bar{3}m$ | A1 | 3.61 ^b | 3.61 ^b | 3.61 ^b | 8.97 | | 0 |
| | | | 3.52 | 3.52 | 3.52 | | | |
| | | | 3.55 ^c | 3.55 ^c | 3.55 ^c | | | |

^a Exp. in [38]; ^b exp. in [24]; ^c exp. in [39].**Figure 2.** Calculated formation enthalpy and cohesive energy of intermetallic compounds in Ti-Co binary system (adopted from [20,23]).

3.2. Elastic Properties

The elastic constants of the Ti-Co binary compounds phase were evaluated according to the method adopted by Wang and Ye [40]. By applying a series of strain values ($\delta = \pm 0.03, \pm 0.06, \pm 0.09, \pm 0.012, \pm 0.015$ and ± 0.018), the elastic constant was derived by quadratic polynomial fitting to the resulting total energy change. Table 2 shows the elastic constants (C_{ij}) of five Ti-Co compounds. The calculated results were in good agreement with the previous experiments [26,41]. According to Bob-Huang's lattice dynamics theory [42,43], the crystals are mechanically stable only if $C_{11} > 0$, $C_{44} > 0$, $C_{11} > |C_{12}|$ and $(C_{11} + 2C_{12}) > 0$ for cubic crystal systems (i.e., Ti₂Co, TiCo, TiCo₂(c), TiCo₃) and $C_{44} > 0$, $C_{11} > |C_{12}|$ and $(C_{11} + 2C_{12})C_{33} > 2C_{13}^2$ for hexagonal systems (i.e., TiCo₂(h)). Table 2 shows that the elastic constants of the five compounds all met the corresponding stability criteria, indicating that they are mechanically stable.

Table 2. Calculated elastic constants of Ti-Co binary compounds.

| Phases | C ₁₁ (GPa) | C ₁₂ (GPa) | C ₁₃ (GPa) | C ₃₃ (GPa) | C ₄₄ (GPa) |
|-----------------------|-----------------------|-----------------------|-----------------------|-----------------------|-----------------------|
| Ti ₂ Co | 155.0 | 128.7 | | | 85.8 |
| TiCo | 220.1 | 137.9 | | | 70.3 |
| | 203 ^a | 129 ^a | | | 68 ^a |
| TiCo ₂ (c) | 280.0 | 135.1 | | | 100.4 |
| TiCo ₂ (h) | 358.8 | 131.7 | 118.9 | 366.0 | 93.8 |
| TiCo ₃ | 236.2 | 149.1 | | | 113.7 |
| | 228 ^a | 148 ^a | | | 129 ^a |

^a Exp. in [26].

Using the elastic matrices of single crystals, the bulk modulus (B), shear modulus (G), Young's modulus (E) and Poisson's ratio (ν) of polycrystals can be calculated via the Voigt–Reuss–Hill (VRH) scheme [44]. For cubic crystal systems [42]:

$$B_V = B_R = \frac{C_{11} + 2C_{12}}{3} \quad (3)$$

$$G_V = \frac{(C_{11} - C_{12} + 3C_{44})}{5} \quad (4)$$

$$G_R = \frac{5(C_{11} - C_{12})C_{44}}{4C_{44} + 3(C_{11} - C_{12})} \quad (5)$$

For hexagonal crystal systems [42]:

$$B_V = \frac{2(C_{11} + C_{12}) + 4C_{13} + C_{33}}{9} \quad (6)$$

$$G_V = \frac{M + 12C_{44} + 12C_{66}}{30} \quad (7)$$

$$B_R = \frac{C^2}{M} \quad (8)$$

$$G_R = \frac{5(C^2 C_{44} C_{66})}{2[3B_V C_{44} C_{66} + C^2(C_{44} + C_{66})]} \quad (9)$$

$$M = C_{11} + C_{12} + 2C_{33} - 4C_{13} \quad (10)$$

$$C^2 = (C_{11} + C_{12})C_{33} - 2C_{13}^2 \quad (11)$$

The bulk modulus (B), shear modulus (G), Young's modulus (E) and Poisson's ratio (ν) can be calculated by [42]:

$$B_{VRH} = \frac{(B_V + B_R)}{2} \quad (12)$$

$$G_{VRH} = \frac{(G_V + G_R)}{2} \quad (13)$$

$$E = \frac{9B_{VRH}G_{VRH}}{3B_{VRH} + G_{VRH}} \quad (14)$$

$$\nu = \frac{3B_{VRH} - 2G_{VRH}}{2(3B_{VRH} + G_{VRH})} \quad (15)$$

where V and R were calculated using the Voigt and Reuss methods, respectively. After the bulk and shear modulus are obtained, the Vickers hardness H_v can be estimated by the empirical formula proposed by Chen [45]:

$$H_v = 2 \left(K^2 G \right)^{0.585} - 3 \quad (16)$$

where K is the Proctor ratio (i.e., G_{VRH}/B_{VRH}). The shear modulus (G), bulk modulus (B), Young's modulus (E), Poisson's ratio (ν), B/G ratio and Vickers hardness (H_V) of the compounds are shown in Table 3. For polycrystals, the bulk modulus of solids reflects the atomic bonding strength [46]. $\text{TiCo}_2(\text{h})$ has the highest bulk modulus, and Ti_2Co has the lowest bulk modulus, indicating that the $\text{TiCo}_2(\text{h})$ exhibits the highest atomic bond strength. The shear modulus represents the relationship between reversible deformation resistance and shear stress [47]. $\text{TiCo}_2(\text{h})$ has the highest shear modulus and exhibits the highest reversible deformation resistance, followed by $\text{TiCo}_2(\text{c})$, while Ti_2Co presents the lowest reversible deformation resistance. In general, compounds with small B/G ratios (less than 1.75) are usually brittle, while compounds with higher B/G ratios (greater than 1.75) show more ductility [48]. All Ti-Co compounds have a B/G greater than 1.75, indicating that Ti-Co compounds show strong metallic characters and good ductility. Young's modulus is a physical quantity used to measure the stiffness of a material [49]. Therefore, $\text{TiCo}_2(\text{h})$ has the highest hardness value. Meanwhile, Poisson's ratio is also used to assess the brittleness and ductility of compounds, where the compounds exhibit ductility for ν values higher than 0.26 and brittleness for values lower than 0.26. Poisson's ratios of these five compounds are greater than 0.26, indicating that they are all ductile compounds. In conclusion, Ti-Co binary compounds show good toughness and ductility.

Table 3. Polycrystalline bulk modulus (B_{VRH}), shear modulus (G_{VRH}), Young's modulus (E), Poisson's ratio (ν), B/G ratio and Vickers hardness (H_V) of Ti-Co binary compounds.

| Phase | $B_{VRH}(\text{GPa})$ | $G_{VRH}(\text{GPa})$ | $E(\text{GPa})$ | ν | B/G | $H_V(\text{GPa})$ |
|---------------------------|-----------------------|-----------------------|-----------------|-------|-------|-------------------|
| Ti_2Co | 137.5 | 41.7 | 113.7 | 0.362 | 3.294 | 1.397 |
| TiCo | 165.3 | 56.7 | 152.6 | 0.346 | 2.916 | 3.066 |
| $\text{TiCo}_2(\text{c})$ | 183.4 | 88.1 | 227.8 | 0.293 | 2.082 | 8.649 |
| $\text{TiCo}_2(\text{h})$ | 202.5 | 99.3 | 256.0 | 0.289 | 2.039 | 9.798 |
| TiCo_3 | 178.1 | 77.4 | 202.8 | 0.310 | 2.302 | 6.601 |

The Debye temperature is related to some physical properties of compound, such as elasticity, hardness and specific heat. In addition, sound velocity can be used to evaluate the thermochemical properties and bonding behavior of compounds [50]. The Debye temperature is calculated by [51]:

$$\Theta_D = \frac{h}{k_B} \left[\frac{3n}{4\pi} \left(\frac{N_A \rho}{M} \right) \right]^{1/3} v_m \quad (17)$$

where h is Planck's constant, k_B is Boltzmann's constant, N_A is Avogadro's constant, n is the number of atoms per unit, ρ is the density of the compound, M is the molecular weight and v_m is the average speed of sound. The average sound velocity v_m , longitudinal sound velocity v_l and transverse sound velocity v_t are calculated by [51]:

$$v_m = \left[\frac{1}{3} \left(\frac{2}{v_t^3} + \frac{1}{v_l^3} \right) \right]^{-1/3} \quad (18)$$

$$v_l = \left[\frac{\left(B + \frac{4}{3}G \right)}{\rho} \right]^{1/2} \quad (19)$$

$$v_t = \left(\frac{G}{\rho} \right)^{1/2} \quad (20)$$

The calculated values of Debye temperature and sound velocity of five Ti-Co binary compounds are shown in Table 4. It is generally believed that Debye temperature reflects the chemical bonding strength in the crystal structure [52]. Debye temperatures of $\text{TiCo}_2(\text{c})$

and $\text{TiCo}_2(\text{h})$ are higher than those of other compounds, so the bonding strength and stiffness of these two compounds are greater. Meanwhile, the higher Debye temperature means greater relevant thermal conductivity. Therefore, $\text{TiCo}_2(\text{c})$ and $\text{TiCo}_2(\text{h})$ have better thermal conductivity than the other compounds do.

Table 4. Longitudinal sound velocity (v_l , m/s), transverse sound velocity (v_t , m/s), average sound velocity (v_m , m/s) and Debye temperature (Θ_D , K) of Ti-Co binary compounds.

| Phase | Θ_D | v_m | v_l | v_t |
|---------------------------|------------|-------|-------|-------|
| Ti_2Co | 366.4 | 3.016 | 5.760 | 2.678 |
| TiCo | 411.3 | 3.266 | 5.991 | 2.906 |
| $\text{TiCo}_2(\text{c})$ | 494.0 | 3.820 | 6.325 | 3.423 |
| $\text{TiCo}_2(\text{h})$ | 519.4 | 3.942 | 6.491 | 3.534 |
| TiCo_3 | 388.0 | 3.285 | 5.600 | 2.937 |

3.3. Mechanical Anisotropy

Crystals can show different physical and chemical properties in different directions. The microcracks and lattice distortion in materials are usually closely related to the mechanical anisotropy of materials [53,54]. Therefore, the general elastic anisotropy index (A^U), isotropic percentage of compressibility (A_G and A_B) and shear anisotropy factor (A_1 , A_2 and A_3) of all Ti-Co binary compounds were calculated by [53]:

$$A^U = 5 \frac{G_V}{G_R} + \frac{B_V}{B_R} - 6 \geq 0 \quad (21)$$

$$A_B = \frac{G_B - G_B}{G_B + G_B} \times 100\% \quad (22)$$

$$A_G = \frac{G_V - G_R}{G_V + G_R} \times 100\% \quad (23)$$

$$A_1 = \frac{4C_{44}}{C_{11} + C_{33} - 2C_{13}} \text{ for (100) plane} \quad (24)$$

$$A_2 = \frac{4C_{55}}{C_{22} + C_{33} - 2C_{23}} \text{ for (010) plane} \quad (25)$$

$$A_3 = \frac{4C_{66}}{C_{11} + C_{22} - 2C_{12}} \text{ for (001) plane} \quad (26)$$

where, B_V , B_R , G_V and G_R are the shear modulus and bulk modulus calculated using the Voigt and Reuss methods.

Ranganathan et al. [54] used A^U to describe the anisotropy of materials. The greater the value of A^U is, the greater the mechanical anisotropy of the materials is. The materials with A^U of 0 are generally considered to be isotropic. The values of anisotropy index are shown in Table 5. In comparing the values of A^U , Ti_2Co has the strongest mechanical anisotropy, followed by TiCo_3 , which also exhibits strong mechanical anisotropy. $\text{TiCo}_2(\text{h})$ shows the lowest mechanical anisotropy. In addition, A_G can be used to evaluate the elastic anisotropy of materials in shear mode. Ti_2Co had the largest A_G value of 0.3596%, indicating that Ti_2Co exhibits the strongest shear modulus anisotropy, and $\text{TiCo}_2(\text{h})$ exhibits the lowest shear modulus anisotropy, with an A_G value of 0.0064%. The general elastic anisotropy and shear modulus anisotropy followed the same trend in the Ti-Co binary compounds. The order of mechanical anisotropy of Ti-Co compounds is $\text{Ti}_2\text{Co} > \text{TiCo}_3 > \text{TiCo} > \text{TiCo}_2(\text{c}) > \text{TiCo}_2(\text{h})$. The values of A^U and A_G indicate that the mechanical properties of Ti-Co binary compounds are anisotropic. To understand the mechanical anisotropy of Ti-Co binary compounds more intuitively, the three-dimensional model was used to describe the mechanical modulus. Using the code developed by Romain et al. [55], the elastic constant can be used to draw the three-dimensional anisotropic

function of Young's modulus of Ti-Co binary compounds. The cubic crystal systems are the most symmetrical ones among all crystal systems, and their Young's moduli in any direction can be expressed as:

$$\frac{1}{E} = S_{11} - 2\left(S_{11} - S_{12} - \frac{S_{44}}{2}\right)(l_1^2 l_2^2 + l_2^2 l_3^2 + l_1^2 l_3^2) \quad (27)$$

hexagonal crystal systems can be expressed as:

$$\frac{1}{E} = S_{11}(1 - l_3^2)^2 + S_{33}l_3^4 + (S_{44} + 2S_{13})(1 - l_3^2)l_3^2 \quad (28)$$

where l_1 , l_2 and l_3 are the direction cosines, and S_{ij} is the elastic compliance constants. In spherical coordinates, $l_1 = \sin\theta\cos\varphi$, $l_2 = \sin\theta\sin\varphi$ and $l_3 = \cos\theta$, and the three-dimensional surface of Young's modulus of Ti-Co binary compounds can be drawn (Figure 3). The Young's modulus of five Ti-Co binary compounds is anisotropic. Ti_2Co had the most anisotropic Young's modulus, while the contour of $\text{TiCo}_2(\text{h})$ Young's modulus was spherical, showing a smallest anisotropic Young's modulus. The anisotropy of Young's modulus of the other three compounds was between those of $\text{TiCo}_2(\text{h})$ and Ti_2Co . Considering the crystal structure of $\text{TiCo}_2(\text{h})$ (hexagonal lattice), the isotropic Young's modulus of $\text{TiCo}_2(\text{h})$ is easy to understand. However, Ti_2Co is a complex face-centered cubic phase, so it showed a more anisotropic profile of Young's modulus.

Table 5. Calculated shear anisotropy factors (A_1 , A_2 and A_3), universal anisotropy index (A^U) and anisotropy index (A_B and A_C) of the Ti-Co binary compounds.

| Phase | A^U | A_G | A_1 | A_2 | A_3 |
|---------------------------|--------|--------|--------|--------|--------|
| Ti_2Co | 5.5247 | 0.3596 | 6.5247 | 6.5247 | 6.5247 |
| TiCo | 1.7105 | 0.0348 | 1.7105 | 1.7105 | 1.7105 |
| $\text{TiCo}_2(\text{c})$ | 1.3858 | 0.0127 | 1.3816 | 1.3816 | 1.3816 |
| $\text{TiCo}_2(\text{h})$ | 0.8261 | 0.0064 | 0.7704 | 0.7704 | 0.8261 |
| TiCo_3 | 2.6108 | 0.1066 | 2.6108 | 2.6108 | 2.6108 |

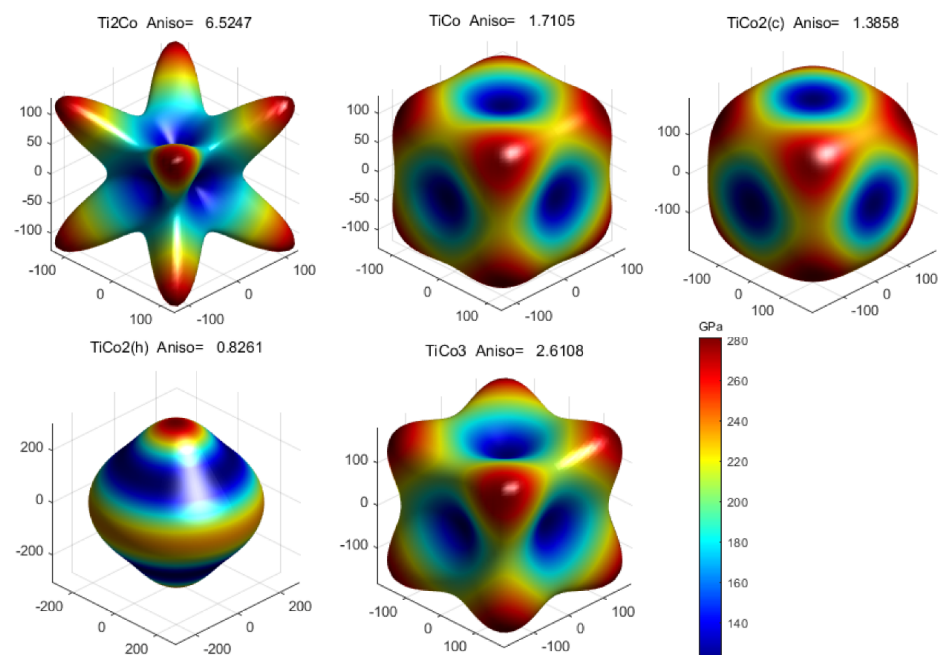


Figure 3. Surface constructions of Young's modulus of Ti-Co binary compounds in three-dimensional space.

3.4. Phonon Properties

Phonon dispersion can accurately reveal the phonon behavior of crystal structure [56]. The phonon spectra and the density of states of five structures of Ti-Co binary compounds were calculated by the supercell method. The force constants were calculated in the finite displacement method [30] using the PHONOPY code [57]. The phonon spectra of Ti-Co binary compounds along the highly symmetric path and the corresponding projected phonon density of states are shown in Figure 4. All five compounds show no imaginary frequencies throughout the Brillouin zone and can, therefore, be shown to be thermodynamically stable. These five compounds basically vibrate in the frequency range of 0–12 THz. It is obvious that the frequency range of $\text{TiCo}_2(\text{c})$ and $\text{TiCo}_2(\text{h})$ is wider than that of other compounds. The highest frequency of $\text{TiCo}_2(\text{c})$ and $\text{TiCo}_2(\text{h})$ can reach up to 12 THz. For both alloys, the Co atom vibrates in the full frequency range and the Ti atom vibrates in the range of 0–8 THz. The C atom has an important contribution in all phonon modes, whereas the O atom mainly plays a role in the low frequency region and the intermediate frequency region. For TiCo_3 , the Co atom also vibrates in the full frequency range, but the Ti atom mainly vibrates the high frequency region. For Ti_2Co and TiCo , the Ti atom mainly vibrates in the high-frequency region and Co atom mainly vibrates in the low-frequency region. In general, the vibration frequency of Ti atom is higher than that of Co atom, mainly because the atomic mass of Ti atom is greater than that of Co atom.

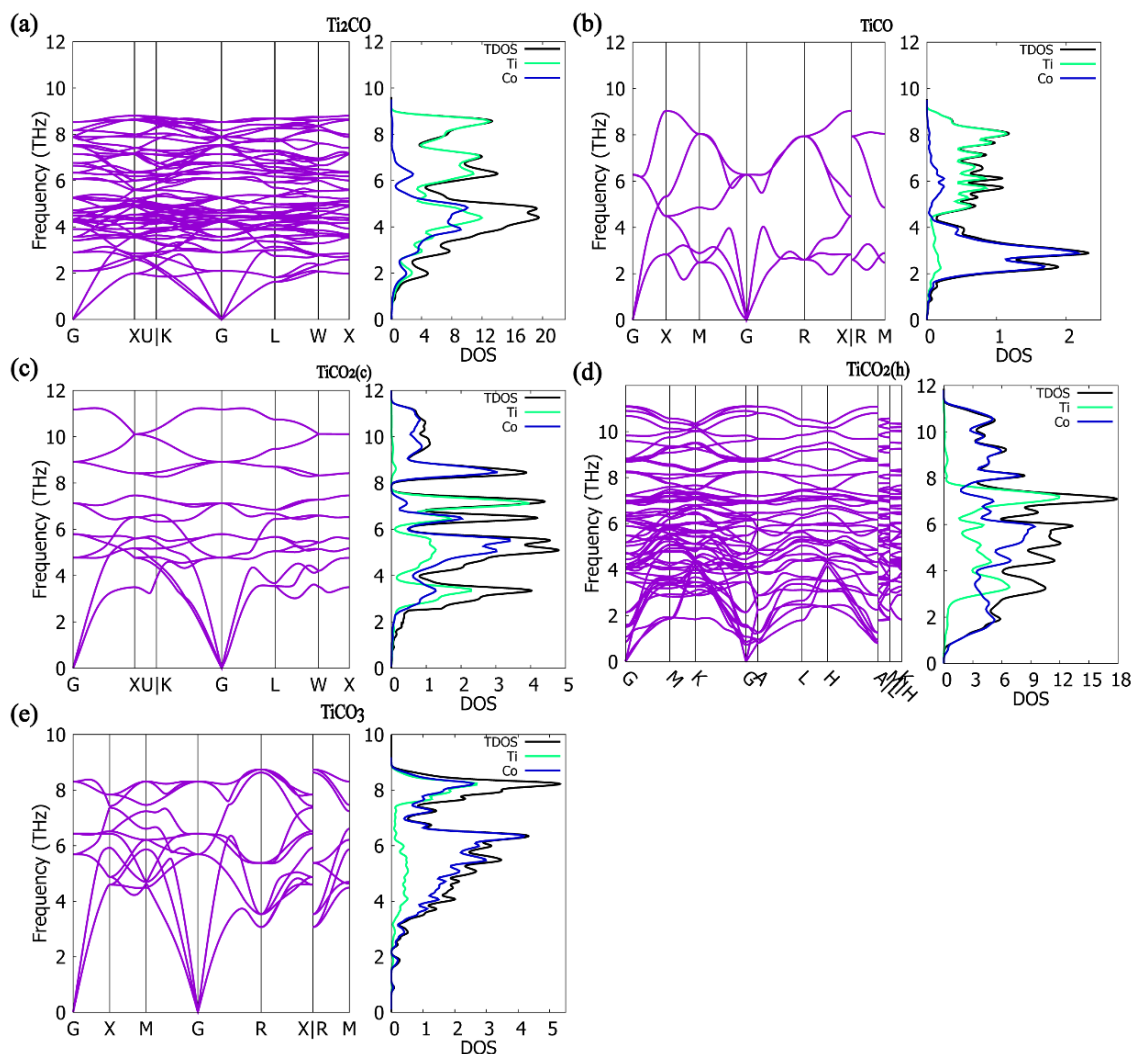


Figure 4. Phonon dispersion and density of states of Ti-Co binary compounds: (a) Ti_2Co ; (b) TiCo ; (c) $\text{TiCo}_2(\text{c})$; (d) $\text{TiCo}_2(\text{h})$; (e) TiCo_3 .

3.5. Bonding Characteristic

To understand the bonding characteristics of Ti-Co binary compounds, the total density of state (TDOS) and partial density of state (PDOS) of the five compounds are shown in Figure 5. Spin polarization was considered in the calculations. For all five compounds, the spin-up and spin-down TDOS at Fermi energy (E_F) levels are greater than zero, which means that these compounds have metallic features. Interestingly, the Fermi energy level of TiCo_3 is located at the top of the valence band in the spin-up region, which is a semi-metallic property. In addition, TDOS has a deep valley close to the Fermi level in every Ti-Co compound, which is called pseudo energy gap. It is generally believed that the pseudo energy gap reflects the strength of covalent-like bonds of the system [58]. The wider the pseudo energy gap is, the stronger the covalence is. Thus, the covalent-like bonding of TiCo and Ti_2Co are relatively strong, while the covalent-like bonds of $\text{TiCo}_2(\text{h})$ and $\text{TiCo}_2(\text{c})$ are relatively weak. It is generally believed that the stronger the covalent-like bond is, the more stable the compound is [58]. Therefore, TiCo and Ti_2Co are more stable, while $\text{TiCo}_2(\text{h})$ and $\text{TiCo}_2(\text{c})$ are less stable. This is in good agreement with the calculated formation enthalpies. DOS near the Fermi level mainly contributes to the directional chemical bonding between Ti atoms and Co atoms. The local density of states of Fermi level also mainly comes from d of Ti and Co atoms. On the contrary, Ti- s , p and Co- s , p states have no obvious contribution. Therefore, strong d - d hybridization is the main reason for the formation of the pseudo energy gap, and the covalent-like bond of Ti-Co alloy is also derived from d - d electron interaction. As the Co content increases, the proportion of Co- d at Fermi level also increases.

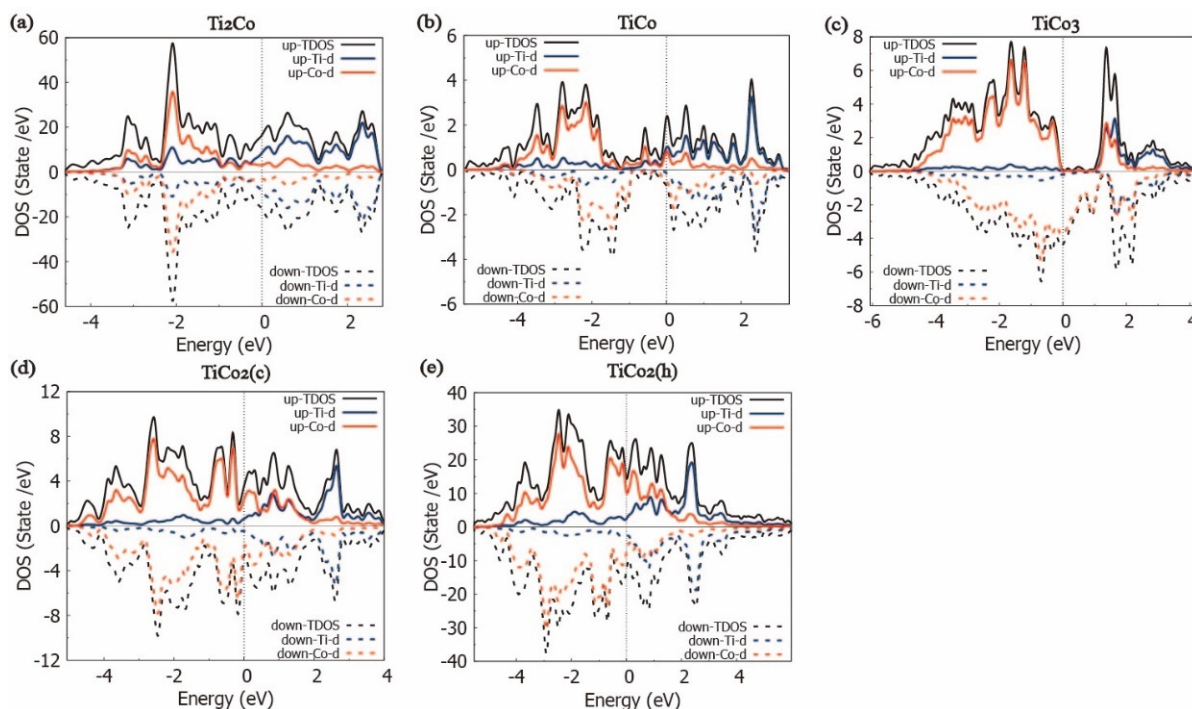


Figure 5. Density of states of Ti-Co binary compounds: (a) Ti_2Co ; (b) TiCo; (c) TiCo_3 ; (d) $\text{TiCo}_2(\text{c})$; (e) $\text{TiCo}_2(\text{h})$.

Due to Co atoms, most Ti-Co binary compounds are spin polarized [59]. The degree of polarization can be calculated by the fractional difference between the two spin states of the Fermi level (E_F) [60]:

$$P = \frac{N_{\uparrow}(E_F) - N_{\downarrow}(E_F)}{N_{\uparrow}(E_F) + N_{\downarrow}(E_F)} \quad (29)$$

where $N_{\uparrow}(E_F)$ and $N_{\downarrow}(E_F)$ represent DOS with Fermi-level spin-up and spin-down, respectively. When P is zero, it indicates paramagnetic and antiferromagnetic properties [60].

When P is non-zero, it indicates ferromagnetic properties. So, TiCo and TiCo₂(h) show obvious ferromagnetism; the DOS values of Ti₂Co and TiCo₂(c) spin-up and spin-down are symmetrical, so these two compounds are non-magnetic. Conversely, in the spin-up DOS of TiCo₃, there is a section of the energy gap, and the Fermi energy level intersects the spin-down DOS and is in the energy range of the spin-up DOS. Thus, TiCo₃ is spin polarized, and it exhibits ferrimagnetism.

In addition, the differential charge density distribution is defined as the electron difference between an isolated atom and its bonding state, which gives information about the bonding properties [61]. The atomic (001) plane was chosen to illustrate the electron transfer properties of Ti-Co binary compounds in Figure 6. The shape characteristics of the differential charge density distributions around Ti and Co atoms show that the charge is mainly transferred from Co atoms to Ti atoms. Therefore, the binding mode of Ti-Co compounds is mainly determined by the Ti-Co bond. Some electrons are clearly out of domain in the interstitial region between Ti and Co atoms, implying the presence of metal and covalent-like bonds. For TiCo and TiCo₃, there is a cross-shaped, red region around the Ti atoms, which means that the Ti atoms forms bonds with the Co atoms within this region. For Ti₂Co, TiCo₂(h) and TiCo₂(c), a triangular red region forms around the Ti atom, indicating that Ti and Co atoms are mainly covalently bonded to each other. The more electron interactions there are between atoms in a compound composed of transition metals, the more stable the crystal structure is. The accumulation of a large number of electrons between adjacent atoms in TiCo, with large electron interactions, makes TiCo the most stable phase. This result is consistent with the enthalpy results. In addition, the charge transfer in Ti₂Co indicates the highest binding force, which is consistent with the cohesion energy.

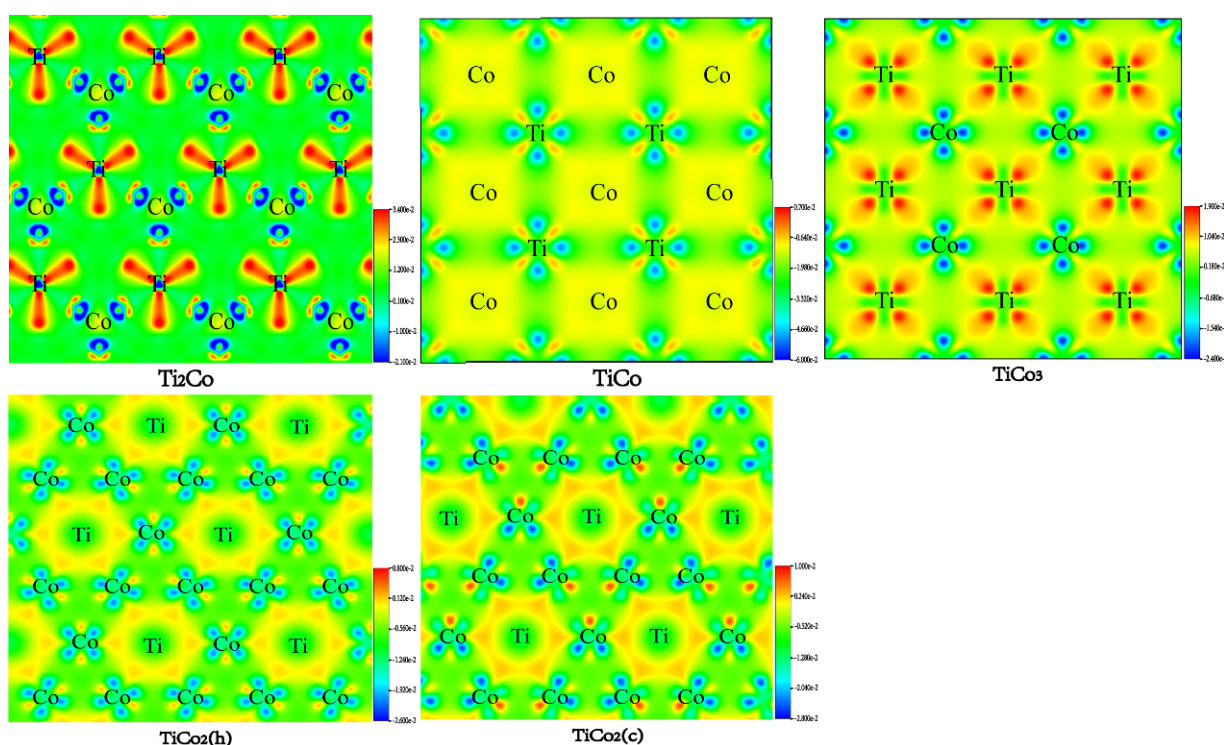


Figure 6. Differential charge density distributions of Ti-Co binary compounds on the (001) plane. The red area shows electron surplus, and the blue area shows electron deficiency.

3.6. Slip Properties

The GSFE curve for the slip system provides an indication of the plastic deformation behaviors of the alloy [31]. Mulay et al. [61] studied the deformation mechanism in the B₂-type phase (TiCo) through the analysis of $g \cdot b$ using the transmission electron micro-

scope and the grain orientation axis (IGMA) obtained by electron backscatter diffraction and found that $\{011\}\langle 100\rangle$ and $\{001\}\langle 100\rangle$ are the main slip systems under low stress. In the process of strain hardening transformation, the secondary slip mechanism is activated and three slip systems, $\{1\bar{1}0\}\langle 111\rangle$, $\{110\}\langle 001\rangle$ and $\{1\bar{1}0\}\langle 110\rangle$, are generated, thus providing five independent slip systems, which meet the von Mises criterion of polycrystalline ductility [62]. The L_{12} -type phase (TiCo_3) is an ordered face-centered cubic structure. For this phase, slip mainly occurs on the $\{111\}$ plane. Previous studies have shown that the L_{12} -type phase will generate antiphase boundaries (APB), superlattice intrinsic stacking faults (SISF) and composite stacking faults (CSF) on the $\{111\}$ plane [63,64]. By sliding on the $\{111\}$ plane, a perfect $a\{1\bar{1}0\}\langle 111\rangle$ dislocation can be dissociated into two $a/2\{1\bar{1}0\}\langle 111\rangle$ partial dislocations and one APB energy value or into two $a/3\{111\}\langle \bar{2}11\rangle$ partial dislocations and one SISF energy value. It can be expressed as [63,64]:

$$a[1\bar{1}0] \rightarrow a/2[1\bar{1}0] + APB + a/2[1\bar{1}0] \quad (30)$$

$$a[1\bar{1}0] \rightarrow a/3[\bar{2}11] + SISF + a/3[\bar{2}11] \quad (31)$$

the $a/2\{1\bar{1}0\}\langle 111\rangle$ partial dislocations can be further dissociated into two $a/6\{111\}\langle \bar{2}11\rangle$ partial dislocations to form CSF energy, which can be expressed as [63,64]:

$$a[1\bar{1}0] \rightarrow 6/a[\bar{1}2\bar{1}] + CSF + 6/a[\bar{2}11] + APB + 6/a[\bar{1}2\bar{1}] + CSF + 6/a[\bar{2}11] \quad (32)$$

For Ti_2Co and Laves phase C15-type $\text{TiCo}_2(\text{c})$ alloys with fcc structures, only the slip system $\{110\}\langle 111\rangle$ common to FCC structure was considered [65,66]. One $\{1\bar{1}0\}\langle 111\rangle$ dislocation can be dissociated into two $\{1\bar{1}0\}\langle 111\rangle$ partial dislocations and one intrinsic stacking fault (ISF), which is expressed as:

$$a[1\bar{1}0] \rightarrow a/2[1\bar{1}0] + ISF + a/2[1\bar{1}0] \quad (33)$$

Hexagonal Laves phase C36 undergoes plastic deformation on different slip systems. It is able to slip along the basal plane $\{0001\}$, prismatic plane $\{1\bar{1}00\}$ and pyramidal plane $\{1\bar{1}01\}$ under the slip system, and it may also cross-slip to different slip systems [65,67]. Among them, the GSFE associated with $\text{TiCo}_2(\text{h})$ in the basal and prismatic planes is calculated.

GSFE is defined as the fault energy related to the rigid displacement of one half of an ideal crystal relative to the other half along the Bernstein vector on the slip plane [68]. Under periodic boundary conditions, a fault plane can be generated by the rigid movement of part of a supercell. GSFE was calculated according to different slip systems along a specific slip direction, as shown in the Figure 7. The GSFE (E_{GSF}) value was calculated by [69]:

$$E_{GSF} = \frac{E_u - E_0}{S} \quad (34)$$

where E_u is the total energy of the supercell after sliding vector u along the slip plane (from 0.1 to 1.0; the step size is 0.1), E_0 is the total energy of the perfect supercell and S is the cross-sectional area of the slip plane. In the GSFE calculation, the atoms were fixed along the x and y directions and completely relaxed along the z direction to obtain a reasonable and stable energy value. Meanwhile, there was a 10 Å vacuum region along the slip plane (z direction).

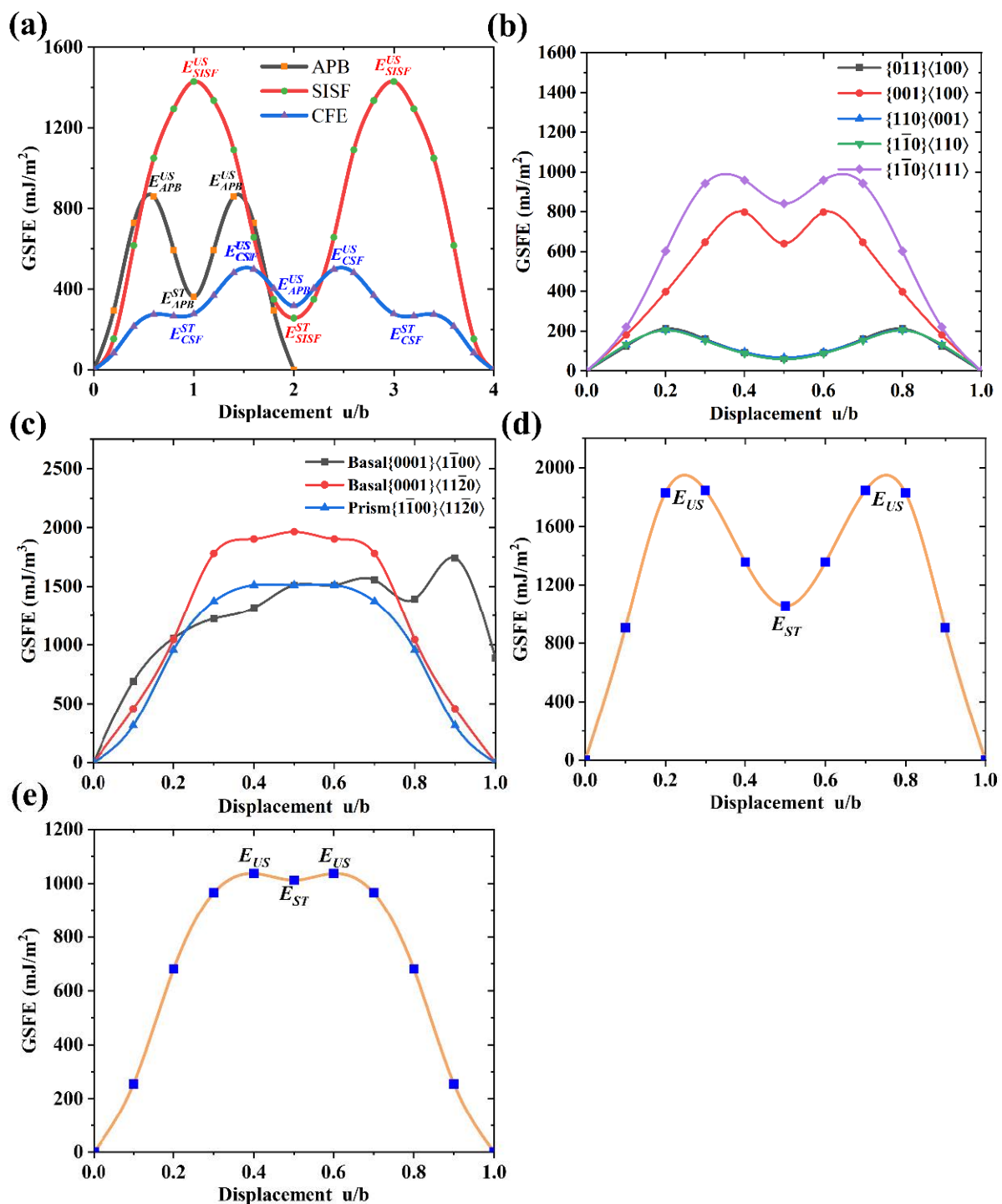


Figure 7. Calculated GSFE curves of the Ti-Co binary compounds: (a) TiCo₃; (b) TiCo; (c) TiCo₂(h); (d) TiCo₂(c); (e) Ti₂Co.

Figure 7a shows that different energy distributions of GSFE obtained by sliding along the {111} plane of TiCo₃ in different directions, and the calculated results are in good agreement with the previous work [70]. It shows that the plane defect on the {111} plane is shown as $E_{APB} > E_{CSF} > E_{SISF}$, and it has a high slip energy barrier (unstable stacking fault energy E_{GSF}^{US}) and plane defect energy (stable stacking fault energy E_{GSF}^{ST}), which gives the L1₂-type alloy TiCo₃ more strength. The complex slip mode is also the reason for the high ductility of TiCo₃. Figure 7b shows the distribution of GSFE of B₂-type alloy TiCo. These five slip systems are the most important independent slip systems of TiCo, meeting the von

Mises criterion of polycrystalline ductility. The slip energy barrier and plane defect energy of these five slip systems are relatively low, especially for the three slip systems, $\{011\}\langle 100\rangle$, $\{110\}\langle 001\rangle$ and $\{1\bar{1}0\}\langle 110\rangle$; the slip energy barrier is about 210 mJ/m^3 , while the plane defect energy is only about 60 mJ/m^3 . In B_2 -type intermetallic compounds, such as Co-Zr, Ti-Co [27], Ag-Y and Cu-Y [71], all exhibit good ductility, while the low slip barrier and planar defects in the slip system of TiCo can provide a satisfactory explanation for the high ductility observed in TiCo. Figure 7c shows the partial slip systems of $\text{TiCo}_2(\text{h})$. Figure 7d,e show the slip of $\text{TiCo}_2(\text{c})$ and Ti_2Co on the $\{111\}$ plane, respectively, which is the most common slip mode of face-centered cubic structure. It is shown that the slip barrier and plane defect energy of $\text{TiCo}_2(\text{c})$ are both very high, indicating that dislocation movement of $\text{TiCo}_2(\text{c})$ crystal structure is quite difficult, which increases the strength of $\text{TiCo}_2(\text{c})$.

4. Conclusions

In this work, the phase stability, mechanical properties, bonding characteristics and slip properties of five Ti-Co binary compounds (Ti_2Co , TiCo, $\text{TiCo}_2(\text{c})$, $\text{TiCo}_2(\text{h})$ and TiCo_3) were systematically studied using the first-principles calculation. The following conclusions can be drawn:

- (1) According to thermodynamic and the elastic standards and phonon properties calculated by the frozen phonon method, the five Ti-Co compounds are thermodynamically stable, and TiCo has the lowest enthalpy of formation and is the most stable phase.
- (2) Ti_2Co shows the strongest anisotropy, and $\text{TiCo}_2(\text{h})$ has the weakest anisotropy. The three-dimensional surface of the general anisotropy index and Young's modulus indicate that the magnitude relationship of mechanical anisotropy is $\text{Ti}_2\text{Co} > \text{TiCo}_3 > \text{TiCo} > \text{TiCo}_2(\text{c}) > \text{TiCo}_2(\text{h})$.
- (3) The calculations of bonding characteristic and differential charge density distributions show that Ti-Co compounds are composed of metallic and covalent-like bonds. TiCo shows stronger covalent-like bonding characteristics. Additionally, TiCo and $\text{TiCo}_2(\text{h})$ are ferromagnetic, TiCo_3 is ferromagnetic, and Ti_2Co and $\text{TiCo}_2(\text{c})$ are non-magnetic.
- (4) The calculated stacking fault energy of the slip systems shows that the anomalous ductility of Ti-Co compounds mainly comes from the complex slip systems and the lower slip energy barrier of the compounds.

Author Contributions: Conceptualization, F.Z., B.L. and J.H.; methodology, F.Z., B.L. and J.H.; software, F.Z. and J.H.; validation, F.Z. and H.P.; investigation, M.C. and H.W.; writing—original draft preparation, F.Z.; writing—review and editing, F.Z., B.L. and J.H.; visualization, F.Z.; supervision, B.L. and J.H.; project administration, J.H.; funding acquisition, J.H. All authors have read and agreed to the published version of the manuscript.

Funding: This research was funded by the National Natural Science Foundation of China (Grant No. 51971237) and the Science and Technology Committee of Shanghai Municipal (Grant No. 22ZR1471400).

Data Availability Statement: All data generated or analyzed during this study are included in this published article.

Acknowledgments: Thanks to all the authors for their contributions to this article and to the editors for their valuable comments.

Conflicts of Interest: The authors declare no conflict of interest.

References

1. Yeh, C. Preparation of CoTi intermetallics by self-propagating combustion synthesis. *J. Alloy. Compd.* **2005**, *396*, 228–232. [[CrossRef](#)]
2. Zhu, Y.-X.; Li, C.; Liu, Y.-C.; Ma, Z.-Q.; Yu, H.-Y. Effect of Ti addition on high-temperature oxidation behavior of Co–Ni-based superalloy. *J. Iron Steel Res. Int.* **2020**, *27*, 1179–1189. [[CrossRef](#)]
3. Zhou, P.; Gao, X.; Song, D.; Liu, Q.; Liu, Y.; Cheng, J. Role of Ru on the microstructure and property of novel Co–Ti–V Superalloy. *J. Mater. Res.* **2020**, *35*, 2737–2745. [[CrossRef](#)]

4. Yang, H.-K.; Zhou, C.-Y.; Wang, H.; Yang, B. Phase equilibria in Ti-rich portion and thermodynamic re-optimization of Co-Ti system. *J. Iron Steel Res. Int.* **2022**, *29*, 914–924. [\[CrossRef\]](#)
5. Wang, R.; Welsch, G. Evaluation of an experimental Ti-Co alloy for dental restorations. *J. Biomed. Mater. Res. Part B Appl. Biomater.* **2013**, *101*, 1419–1427. [\[CrossRef\]](#)
6. Ruan, J.J.; Liu, X.J.; Yang, S.Y.; Xu, W.W.; Omori, T.; Yang, T.; Deng, B.; Jiang, H.X.; Wang, C.P.; Kainuma, R.; et al. Novel Co-Ti-V-base superalloys reinforced by L12-ordered γ' phase. *Intermetallics* **2018**, *92*, 126–132. [\[CrossRef\]](#)
7. Mutlu, I. Synthesis and characterization of Ti-Co alloy foam for biomedical applications. *Trans. Nonferrous Met. Soc. China* **2016**, *26*, 126–137. [\[CrossRef\]](#)
8. Pang, X.Z.; Hu, J.; Zhan, Y.Z. Microstructural Characteristics of Ti-Co Alloys for Biomedical Applications. *Adv. Mater. Res.* **2013**, *791–793*, 469–473. [\[CrossRef\]](#)
9. Liu, X.; Chen, S.; Tsoi, J.K.; Matinlinna, J.P. Binary titanium alloys as dental implant materials—A review. *Regen. Biomater.* **2017**, *4*, 315–323. [\[CrossRef\]](#)
10. Liu, Q.; Yang, W.; Chen, G. On superplasticity of two phase alpha-titanium-intermetallic Ti-(Co, Ni)-Al alloy. *Acta Metall. Mater.* **1995**, *43*, 3571–3582. [\[CrossRef\]](#)
11. Hu, K.; Huang, X.; Lu, J.; Liu, H.; Cai, G.; Jin, Z. Measurement of phase equilibria in Ti-Co-Pt ternary system. *Calphad* **2018**, *60*, 191–199. [\[CrossRef\]](#)
12. Zeng, Y.; Zhu, L.; Cai, G.; Liu, H.; Huang, J.; Jin, Z. Investigation of phase equilibria in the Ti-Co-Zr ternary system. *Calphad* **2017**, *56*, 260–269. [\[CrossRef\]](#)
13. Fatoba, O.S.; Adesina, O.S.; Popoola, A.P.I. Evaluation of microstructure, microhardness, and electrochemical properties of laser-deposited Ti-Co coatings on Ti-6Al-4V Alloy. *Int. J. Adv. Manuf. Technol.* **2018**, *97*, 2341–2350. [\[CrossRef\]](#)
14. Gromov, D.G.; Mochalov, A.I.; Pugachevich, V.P. CoSi₂ formation in contact systems based on Ti-Co alloy with low cobalt content. *Appl. Phys. A Mater. Sci. Process.* **1995**, *61*, 565–567.
15. Gromov, D.; Mochalov, A.; Pugachevich, V.; Kirilenko, E.; Trifonov, A. Study of phase separation in Ti-Co-N thin films on silicon substrate. *Appl. Phys. A* **1997**, *64*, 517–521. [\[CrossRef\]](#)
16. Han, J.; Yoo, B.; Im, H.J.; Oh, C.-S.; Choi, P.-P. Microstructural evolution of the heat affected zone of a Co-Ti-W alloy upon laser cladding with a CoNiCrAlY coating. *Mater. Charact.* **2019**, *158*, 109998. [\[CrossRef\]](#)
17. Yoo, B.; Im, H.J.; Seol, J.-B.; Choi, P.-P. On the microstructural evolution and partitioning behavior of L12-structured γ' -based Co-Ti-W alloys upon Cr and Al alloying. *Intermetallics* **2018**, *104*, 97–102. [\[CrossRef\]](#)
18. Murray, J.L. The Co-Ti (Cobalt-Titanium) system. *J. Phase Equilibria* **1982**, *3*, 74–85. [\[CrossRef\]](#)
19. Stein, F.; Merali, M.; Watermeyer, P. The Co-Ti system revisited: About the cubic-to-hexagonal Laves phase transformation and other controversial features of the phase diagram. *Calphad* **2019**, *67*, 101681. [\[CrossRef\]](#)
20. Davydov, A.V.; Kattner, U.R.; Josell, D.; Waterstrat, R.M.; Boettinger, W.J.; Blendell, J.E.; Shapiro, A.J. Determination of the CoTi congruent melting point and thermodynamic reassessment of the Co-Ti system. *Met. Mater. Trans. A* **2001**, *32*, 2175–2186. [\[CrossRef\]](#)
21. Xue, Y.; Wang, H. Microstructure and dry sliding wear resistance of CoTi intermetallic alloy. *Intermetallics* **2009**, *17*, 89–97. [\[CrossRef\]](#)
22. Kaneno, Y.; Takasugi, T.; Hanada, S. Tensile property and fracture behavior of hot-rolled CoTi intermetallic compound. *Mater. Sci. Eng. A* **2001**, *302*, 215–221. [\[CrossRef\]](#)
23. Wu, L.; Zeng, Y.; Pan, Y.; Du, Y.; Peng, Y.; Li, H.; Liu, S.; Zhang, L.; Liu, L. Thermodynamic description and simulation of solidification microstructure in the Co-Ti system. *J. Chem. Thermodyn.* **2019**, *142*, 105995. [\[CrossRef\]](#)
24. Cacciamani, G.; Ferro, R.; Ansara, I.; Dupin, N. Thermodynamic modelling of the Co-Ti system. *Intermetallics* **2000**, *8*, 213–222. [\[CrossRef\]](#)
25. Xi, S.; Chen, L.; Bao, L.; Han, J.; Yu, J.; Li, Z.; Xu, W.; Deng, B.; Wang, C.; Liu, X. Effects of alloying elements on the atomic structure, elastic and thermodynamic properties of L12-Co₃(V, Ti) compound. *Mater. Today Commun.* **2021**, *30*, 102931. [\[CrossRef\]](#)
26. Yasuda, H.; Takasugi, T.; Koiwa, M. Elastic Constants of Co₃Ti and CoTi Intermetallic Compounds. *Mater. Trans. JIM* **1991**, *32*, 48–51. [\[CrossRef\]](#)
27. Wollmershauser, J.; Neil, C.; Agnew, S. Mechanisms of Ductility in CoTi and CoZr B2 Intermetallics. *Met. Mater. Trans. A* **2009**, *41*, 1217–1229. [\[CrossRef\]](#)
28. Jin, M.; Miao, N.; Zhao, W.; Zhou, J.; Du, Q.; Sun, Z. Structural stability and mechanical properties of Co₃(Al, M) (M = Ti, V, Cr, Zr, Nb, Mo, Hf, Ta, W) compounds. *Comput. Mater. Sci.* **2018**, *148*, 27–37. [\[CrossRef\]](#)
29. Xu, W.; Han, J.; Wang, Z.; Wang, C.; Wen, Y.; Liua, X.; Zhu, Z. Thermodynamic, structural and elastic properties of Co₃X (X = Ti, Ta, W, V, Al) compounds from first-principles calculations. *Intermetallics* **2012**, *32*, 303–311. [\[CrossRef\]](#)
30. Chaput, L.; Togo, A.; Tanaka, I.; Hug, G. Phonon-phonon interactions in transition metals. *Phys. Rev. B* **2011**, *84*, 094302. [\[CrossRef\]](#)
31. Vitek, V. Intrinsic stacking faults in body-centred cubic crystals. *Philos. Mag.* **1968**, *18*, 773–786. [\[CrossRef\]](#)
32. Kresse, G.; Hafner, J. Ab initio molecular dynamics for liquid metals. *Phys. Rev. B Condens. Matter.* **1993**, *47*, 558–561. [\[CrossRef\]](#)
33. Kresse, G.; Furthmüller, J. Efficient iterative schemes for ab initio total-energy calculations using a plane-wave basis set. *Phys. Rev. B Condens. Matter.* **1996**, *54*, 11169–11186. [\[CrossRef\]](#) [\[PubMed\]](#)
34. Blöchl, P.E. Projector augmented-wave method. *Phys. Rev. B* **1994**, *50*, 17953–17979. [\[CrossRef\]](#) [\[PubMed\]](#)

35. Perdew, J.P.; Burke, K.; Ernzerhof, M. Generalized gradient approximation made simple. *Phys. Rev. Lett.* **1996**, *77*, 3865–3868. [\[CrossRef\]](#)
36. Chadi, D.J. Special points for Brillouin-zone integrations. *Phys. Rev. B* **1977**, *16*, 1746–1747. [\[CrossRef\]](#)
37. Ikehata, H.; Nagasako, N.; Furuta, T.; Fukumoto, A.; Miwa, K.; Saito, T. First-principles calculations for development of low elastic modulus Ti alloys. *Phys. Rev. B* **2004**, *70*, 174113. [\[CrossRef\]](#)
38. Guo, G.Y.; Wang, H.H. Gradient-corrected density functional calculation of elastic constants of Fe, Co and Ni in bcc, fcc and hcp structures. *Chin. J. Phys.* **2000**, *38*, 949–961.
39. Liu, Y.; Chong, X.; Jiang, Y.; Zhou, R.; Feng, J. Mechanical properties and electronic structures of Fe-Al intermetallic. *Phys. B Condens. Matter.* **2017**, *506*, 1–11. [\[CrossRef\]](#)
40. Wang, S.Q.; Ye, H.Q. Ab initio elastic constants for the lonsdaleite phases of C, Si and Ge. *J. Phys. Condens. Matter.* **2003**, *15*, 5307–5314. [\[CrossRef\]](#)
41. Lu, W.; Li, C.; Yi, J.; Li, K. Stability and elastic properties of B2 CoX (X = Ti, Zr and Hf) intermetallic compounds as a function of pressure. *Philos. Mag.* **2017**, *98*, 203–218. [\[CrossRef\]](#)
42. Wu, Z.; Zhao, E.; Xiang, H.; Hao, X.; Liu, X.; Meng, J. Crystal structures and elastic properties of superhard IrN₂ and IrN₃ from first principles. *Phys. Rev. B* **2007**, *76*, 054115. [\[CrossRef\]](#)
43. Patil, S.K.R.; Khare, S.V.; Tuttle, B.R.; Bording, J.K.; Kodambaka, S. Mechanical stability of possible structures of PtN investigated using first-principles calculations. *Phys. Rev. B* **2006**, *73*, 104118. [\[CrossRef\]](#)
44. Anderson, O.L. A simplified method for calculating the debye temperature from elastic constants. *J. Phys. Chem. Solids* **1963**, *24*, 909–917. [\[CrossRef\]](#)
45. Chen, X.-Q.; Niu, H.; Li, D.; Li, Y. Modeling hardness of polycrystalline materials and bulk metallic glasses. *Intermetallics* **2011**, *19*, 1275–1281. [\[CrossRef\]](#)
46. Ozisik, H.; Deligoz, E.; Colakoglu, K.; Surucu, G. Structural and mechanical stability of rare-earth diborides. *Chin. Phys. B* **2013**, *22*, 046202. [\[CrossRef\]](#)
47. Korozlu, N.; Colakoglu, K.; Deligoz, E.; Aydin, S. The elastic and mechanical properties of MB₁₂ (M = Zr, Hf, Y, Lu) as a function of pressure. *J. Alloy. Compd.* **2013**, *546*, 157–164. [\[CrossRef\]](#)
48. Pugh, S.F. XCII. Relations between the elastic moduli and the plastic properties of polycrystalline pure metals. *Lond. Edinb. Dublin Philos. Mag. J. Sci.* **1954**, *45*, 823–843. [\[CrossRef\]](#)
49. Duan, Y.; Huang, B.; Sun, Y.; Peng, M.; Zhou, S. Stability, elastic properties and electronic structures of the stable Zr–Al intermetallic compounds: A first-principles investigation. *J. Alloy. Compd.* **2013**, *590*, 50–60. [\[CrossRef\]](#)
50. Jian, Y.; Huang, Z.; Xing, J.; Sun, L.; Liu, Y.; Gao, P. Phase stability, mechanical properties and electronic structures of Ti Al binary compounds by first principles calculations. *Mater. Chem. Phys.* **2018**, *221*, 311–321. [\[CrossRef\]](#)
51. Feng, J.; Xiao, B.; Zhou, R.; Pan, W.; Clarke, D.R. Anisotropic elastic and thermal properties of the double perovskite slab–rock salt layer Ln₂SrAl₂O₇ (Ln = La, Nd, Sm, Eu, Gd or Dy) natural superlattice structure. *Acta Mater.* **2012**, *60*, 3380–3392. [\[CrossRef\]](#)
52. Tohei, T.; Kuwabara, A.; Oba, F.; Tanaka, I. Debye temperature and stiffness of carbon and boron nitride polymorphs from first principles calculations. *Phys. Rev. B* **2006**, *73*, 064304. [\[CrossRef\]](#)
53. Liu, Y.; Chávez, J.P. Controlling coexisting attractors of an impacting system via linear augmentation. *Phys. D Nonlinear Phenom.* **2017**, *348*, 1–11. [\[CrossRef\]](#)
54. Ranganathan, S.I.; Ostoja-Starzewski, M. Universal Elastic Anisotropy Index. *Phys. Rev. Lett.* **2008**, *101*, 055504. [\[CrossRef\]](#)
55. Gaillac, R.; Pullumbi, P.; Coudert, F.-X. ELATE: An open-source online application for analysis and visualization of elastic tensors. *J. Phys. Condens. Matter.* **2016**, *28*, 275201. [\[CrossRef\]](#)
56. Moreira, E.; Barboza, C.; Albuquerque, E.; Fulco, U.; Henriques, J.; Araújo, A. Vibrational and thermodynamic properties of orthorhombic CaSnO₃ from DFT and DFPT calculations. *J. Phys. Chem. Solids* **2015**, *77*, 85–91. [\[CrossRef\]](#)
57. Togo, A.; Oba, F.; Tanaka, I. First-principles calculations of the ferroelastic transition between rutile-type and CaCl₂-type SiO₂ at high pressures. *Phys. Rev. B* **2008**, *78*, 134106. [\[CrossRef\]](#)
58. Kirihaara, K.; Nagata, T.; Kimura, K.; Kato, K.; Takata, M.; Nishibori, E.; Sakata, M. Covalent bonds and their crucial effects on pseudogap formation in α -Al(Mn,Re)Si icosahedral quasicrystalline approximant. *Phys. Rev. B* **2003**, *68*, 014205. [\[CrossRef\]](#)
59. LeClair, P.; Kohlhepp, J.T.; van de Vin, C.H.; Wieldraaijer, H.; Swagten, H.J.M.; de Jonge, W.J.M.; Davis, A.H.; MacLaren, J.M.; Moodera, J.S.; Jansen, R. Band Structure and Density of States Effects in Co-Based Magnetic Tunnel Junctions. *Phys. Rev. Lett.* **2002**, *88*, 107201. [\[CrossRef\]](#)
60. Soulen, R.J.; Byers, J.M.; Osofsky, M.S.; Nadgorny, B.; Ambrose, T.; Cheng, S.F.; Broussard, P.R.; Tanaka, C.T.; Nowak, J.; Moodera, J.S.; et al. Measuring the Spin Polarization of a Metal with a Superconducting Point Contact. *Science* **1998**, *282*, 85–88. [\[CrossRef\]](#) [\[PubMed\]](#)
61. Wu, J.; Chong, X.; Jiang, Y.; Feng, J. Stability, electronic structure, mechanical and thermodynamic properties of Fe-Si binary compounds. *J. Alloy. Compd.* **2017**, *693*, 859–870. [\[CrossRef\]](#)
62. Mulay, R.; Agnew, S. Hard slip mechanisms in B2 CoTi. *Acta Mater.* **2012**, *60*, 1784–1794. [\[CrossRef\]](#)
63. Wang, J.; Sehitoglu, H. Dislocation slip and twinning in Ni-based L12 type alloys. *Intermetallics* **2014**, *52*, 20–31. [\[CrossRef\]](#)
64. Wang, W.Y.; Xue, F.; Zhang, Y.; Shang, S.-L.; Wang, Y.; Darling, K.A.; Kecskes, L.J.; Li, J.; Hui, X.; Feng, Q.; et al. Atomic and electronic basis for solutes strengthened (010) anti-phase boundary of L12 Co₃(Al, TM): A comprehensive first-principles study. *Acta Mater.* **2017**, *145*, 30–40. [\[CrossRef\]](#)

65. Luo, W.; Kirchlechner, C.; Zavašnik, J.; Lu, W.; Dehm, G.; Stein, F. Crystal structure and composition dependence of mechanical properties of single-crystalline NbCo₂ Laves phase. *Acta Mater.* **2020**, *184*, 151–163. [[CrossRef](#)]
66. Yuan, F.; Li, G.; Liu, C.; Han, F.; Zhang, Y.; Muhammad, A.; Gu, H.; Guo, W.; Ren, J. Cross stacking faults in Zr(Fe,Cr)₂ face-centered cubic Laves phase nanoparticle. *Appl. Surf. Sci.* **2020**, *513*, 145716. [[CrossRef](#)]
67. Guénolé, J.; Mouhib, F.-Z.; Huber, L.; Grabowski, B.; Korte-Kerzel, S. Basal slip in Laves phases: The synchroshear dislocation. *Scr. Mater.* **2019**, *166*, 134–138. [[CrossRef](#)]
68. Shih, M.; Miao, J.; Mills, M.; Ghazisaeidi, M. Stacking fault energy in concentrated alloys. *Nat. Commun.* **2021**, *12*, 3590. [[CrossRef](#)] [[PubMed](#)]
69. Vitek, V.; Paidar, V. Non-planar Dislocation Cores: A Ubiquitous Phenomenon Affecting Mechanical Properties of Crystalline Materials. *Dislocations Solids* **2008**, *14*, 439–514. [[CrossRef](#)]
70. Im, H.J.; Lee, S.; Choi, W.S.; Makineni, S.K.; Raabe, D.; Ko, W.S.; Choi, P.P. Effects of Mo on the mechanical behavior of γ/γ' -strengthened Co-Ti-based alloys. *Acta Mater.* **2020**, *197*, 69–80. [[CrossRef](#)]
71. Russell, A.; Zhang, Z.; Lograsso, T.; Lo, C.; Pecharsky, A.; Morris, J.; Ye, Y.; Gschneidner, K.; Slager, A. Mechanical properties of single crystal YAg. *Acta Mater.* **2004**, *52*, 4033–4040. [[CrossRef](#)]

Disclaimer/Publisher's Note: The statements, opinions and data contained in all publications are solely those of the individual author(s) and contributor(s) and not of MDPI and/or the editor(s). MDPI and/or the editor(s) disclaim responsibility for any injury to people or property resulting from any ideas, methods, instructions or products referred to in the content.